High-fidelity Simulation of High Density-Ratio Liquid Jet Atomization in Crossflow with Experimental Validation

X. Li*, and M. C. Soteriou
United Technologies Research Center
East Hartford, CT 06108 USA

Abstract

Liquid jet atomization in cross-flowing gas is a critical phenomenon in the fuel preparation process and controls combustor efficiency and emissions. Quantitative experimental studies of atomization have been rare due to limited optical access to the near-field dense spray region. High fidelity multiphase flow simulation has shown promise as an alternative approach for scrutinizing the complex physics involved. Computationally, it remains challenging to resolve the wide range of spatial and temporal scales involved and to properly account for the large variation of density across the liquid-gas interface. In this work, the Coupled Level Set and Volume Of Fluid (CLSVOF) approach is used to directly capture liquid-gas interface involving topological changes. The ghost fluid method is used to facilitate simulations at realistic fuel-air density ratio. Adaptive Mesh Refinement (AMR) and Lagrangian droplet models are used to efficiently resolve the multiple scales simultaneously. High performance computing is leveraged to manage the cost of the high resolution simulations which were performed using over 2000 processors at the Oakridge Leadership Computing Facility of the US Department of Energy. The equivalence between uniform resolution and AMR-based simulations is established by comparing surface instability and breakup. The significant cost advantages of using AMR are documented. The detailed simulation results at different Weber numbers are validated with experimental measurements of surface wavelength, breakup location and column trajectory. The size, velocity and mass rate of droplets formed along jet column are studied and also compared with experimental measurements. The effects of increasing Weber number on jet breakup and aerodynamic flow are discussed.

*Corresponding author: lixy2@utrc.utc.com

Introduction

Atomization of fuel jets in cross-flowing air to generate micron-size droplets is critical to the performance of combustors encountered in commercial and military aerospace applications, such as gas turbines, augmentors, scramjets and ramjets and rockets. Increased fuel area-to-volume ratio due to atomization significantly enhances the fuel evaporation rate, which contributes to better fuel-air mixing and subsequent combustion of fuels. While the magnitude of fuel-air ratio has an impact on engine efficiency and emissions, the spatiotemporal distribution of fuel vapor is strongly linked to dynamic stability. Therefore substantial demand exists for the quantitative understanding of liquid atomization in crossflow, as a first step in the optimization of combustion processes.

From the breakup of centimeter-size liquid jet column to pinch-off of micron-size ligaments to form droplets, liquid primary atomization in a crossflowing gas manifests itself as a complex multiphysics multiscale phenomenon. Different dynamic forces due to gas flow, liquid inertia and surface tension compete with each other, controlling the various instabilities that tend to characterize multiphase flows. Near the liquid column, either Rayleigh-Taylor instability due to density difference, or Kelvin-Helmholtz instability due to aerodynamic shear, or the combination of both drives the large scale growth of surface waves and liquid breakup. On the other hand, capillary Plateau-Rayleigh instability due to surface tension plays a dominant role in the pinch-off of highly stretched thin ligaments when their size drops below a certain threshold. Different instability mechanisms selectively dominate the breakup process of jet column at different flow conditions, resulting in different breakup regimes including column breakup, bag breakup, multimode breakup and shear breakup [1, 2]. Various instabilities often occur simultaneously [3] at different spatial locations of the column. As a result, complicated location-specific liquid structures form which critically control the formation and spatial distribution of droplets. The transport and evaporation of these droplets controls the downstream fuel-air profile and hence the combustion process.

Early experimental studies of primary atomization [4-7] focused on large-scale, integral and steady features such as penetration length or liquid column trajectory, mainly because of the limitations of optical techniques in resolving the spatiotemporal evolution of the near-field fast changing spray field. The situation is also complicated by the optical obstruction due to dense spray. Recently, several groups [1, 2, 8] started to use the pulsed shadowgraph technique to obtain more details of the evolution of liquid column. Despite the fact that most analyses are based on processing two-dimensional images, near-field features such as wavelength of liquid surface waves, deformation of liquid column, onset of liquid breakup and deflected trajectory of liquid column were successfully extracted. The breakup of jet column was found similar to the well-studied secondary breakup of drops due to shock wave disturbance [9, 10], and the data were summarized in a series of quantitative correlations [1, 2]. It is worth noting that most experimental studies were conducted at ambient conditions. Liquid properties (such as density, viscosity and surface tension) and therefore the breakup processes are highly dependent upon operating conditions (such as temperature and pressure) [11]. The extremely hostile high-temperature high-pressure environment in aerospace applications, however, makes experimental research prohibitively difficult and costly.

Due to the fact that fundamental mechanisms of primary breakup and atomization remain largely unknown, phenomenological models have been developed to satisfy the needs in engineering applications. Mimicking jet atomization as “blobs” breaking up under harmonic oscillations and Kelvin-Helmholtz instability, two breakup models, the Taylor analogy breakup (TAB) [12, 13] and wave breakup models [14, 15] have been widely used in many engineering CFD computations based on Reynolds Averaged Navier-Stokes (RANS) formulation. A refined version of such models for liquid jet in cross flow has been developed by Madabhushi [16], taking into account special features such as drag, jet bending and flattening. The cost of the RANS based simulation is low and predictions of the model are reasonably good, despite the fact that experimental data must be available a priori for calibration. The applicability of the model in practical operating conditions is still questionable.

With increasing computational power, it has become affordable in many engineering cases to use Large Eddy Simulations (LES) to capture important larger-scale dynamic features with smaller scale physics filtered out in the simulation and modeled separately. While success was achieved mostly when applying LES to dilute sprays [17], the recently developed LES models [18-20] also demonstrated their feasibility to capture dynamic interfacial flows near the jet column. However, the development of physically-sound subgrid models can be challenging as Herrmann and Gorokhovski [21, 22] pointed out that establishing subgrid models still requires fully resolved subscale interface geometry.

Recently, direct numerical simulations based on interface tracking/capturing methods have shown promise in predicting detailed atomization without two-phase subscale models and experimental calibrations. Methods to directly track or capture the dynamic liquid-gas interface and its topological changes include level-set (LS) [23-27], volume-of-fluid (VOF) [28, 29] and front-tracking (FT) [30, 31], as well as their descendants, such as the refined level-set grid (RLSG) method

[32], the Hybrid LSM & Mars (HLSM) method [33, 34], and the coupled level-set and volume-of-fluid (CLSVOF) method [35, 36]. Detailed atomization mechanisms including instability development and ligament/droplet formation [26, 34] have been explored. However, most simulation efforts have been focused on the case of straight jet injected into quiescent air mainly applicable to diesel engine applications. Because of the high cost of such simulations and lack of detailed experimental data, most numerical algorithms were verified in simple numerical tests and then directly applied to simulate complicated atomization cases at high Weber number and Reynolds number without experimental confirmation. One exception is the high fidelity simulation of liquid jet atomization in a realistic swirling flow injector [52], where the prediction of near-field sprays was compared with experimental data.

In this work, we use a hybrid Eulerian-Lagrangian method [38] to investigate liquid jet atomization in crossflow. The computational approach combines the CLSVOF method to track/capture liquid-gas interface, and a Lagrangian droplet transformation/tracking approach [39] to capture small-scale physics using point particles and alleviate the needs of resolving flow inside droplets. The solver also features a Ghost of Fluid (GF) approach [40, 41] to allow sharp variation of properties across the interface, a Multi-Grid Preconditioned Conjugate Gradient (MGPCG) approach for robust and fast pressure solution, and an Adaptive Mesh Refinement (AMR) technique for liquid-gas interface to reduce grid count [42, 43]. The accuracy of CLSVOF method to capture interface evolutions in simplified geometric settings has been tested previously [35]. In this work, the solver is applied to predict the near-field liquid column in greater detail and compare with recent measurements [1] that employed pulsed shadowgraph techniques. It is noted that other numerical methods (e.g. RLSG) have also recently been applied in the high fidelity simulation of liquid jet atomization in crossflow [44] with improved algorithms for handling increased density ratio [45, 46]. However, to the knowledge of the authors, validation of such direct simulations for jet atomization in cross flow at realistic, high density ratio has not been attempted and therefore is the focus of current work.

In the following, mathematical formulation and numerical implementation of the hybrid Eulerian-Lagrangian approach are briefly described in section II. The algorithms for the Eulerian-to-Lagrangian transformation are briefly described and the details can be found in previous work [38]. In Section III, the presentation of results starts with a qualitative description of a typical jet in cross flow case at an intermediate Weber number. The effects of Weber number on near-field column deformation, surface instability, breakup, droplet formation and liquid-gas interactions are studied. The predictions are compared with correlations developed by Sallam et al[1]. The comparison of near-field data between uniform grid simulation and AMR simulations establishes the equivalence between the two configurations in capturing the surface instability and breakup. Finally, a summary is provided in Section IV.

Numerical methods

A. Governing equations

The incompressible flow of Newtonian fluid in the entire domain Ω, which consists of the gas phase Ω_G and the liquid phase Ω_L is governed by the Navier-Stokes equation [35]

$$\frac{\partial \mathbf{u}}{\partial t} + \mathbf{u}\cdot\nabla\mathbf{u} = \frac{1}{\rho}\nabla\cdot(-p\mathbf{I} + 2\mu\mathbf{D}) - \sigma\kappa\nabla H\,, \qquad (1)$$

where p is the pressure, ρ the density, μ the viscosity, $\mathbf{I}$ the identity tensor, $\mathbf{D}$ the deviatoric strain rate tensor, σ the constant interfacial tension, κ the local curvature and H the Heaviside function defined as

$$H(\phi) = \begin{cases} 1 & \phi \geq 0 \\ 0 & \phi < 0 \end{cases}. \qquad (2)$$

Here ϕ is the level set function, which is positive in the liquid phase and negative in the gas phase. The density and viscosity are correspondingly defined as

$$\rho = \rho_L H(\phi) + \rho_G[1 - H(\phi)]$$
$$\mu = \mu_L H(\phi) + \mu_G[1 - H(\phi)]. \qquad (3)$$

The flow is incompressible, i.e.

$$\nabla\cdot\mathbf{u} = 0\,. \qquad (4)$$

The motion of interface follows

$$\frac{\partial\phi}{\partial t} + \mathbf{u}\cdot\nabla\phi = 0\,. \qquad (5)$$

B. Eulerian approaches: CLSVOF, AMR and GF

The CLSVOF method is used to directly capture the evolution of liquid-gas interface. In addition to the evolution equation for level set ϕ, the transport equation for the cell liquid volume fraction (the volume-of-fluid function, F) is also solved. The interface normals used in the VOF reconstruction step are determined from the level set function. The volume fractions and the normals are then used to construct a volume preserving distance function ϕ. Essentially, volume is preserved by implementing a ‘‘local’’ mass correction at every iteration. Second-order accurate curvature is calculated from F by the method of height fraction [35].

The solver is implemented under the framework of adaptive mesh refinement to save computational cost. A detailed description of the block-structured AMR can be found elsewhere [43]. Cells that are crossed by the liquid-gas interface are tagged for refinement. Starting from the base level, boxes (with a minimum size of,

say, 32^3 cells) are combined to cover all the tagged cells within assigned coverage efficiency. This set of blocks with the same grid spacing forms level 1. This level is in turn tagged for refinement at the interface, and the process is repeated until the required grid resolution is achieved. During the simulation, the data on the fine level are either copied from a previous time step or, when the grid structure has changed locally, conservatively interpolated from the underlying coarse level. The interface, however, is always embedded in the finest grid level to avoid gross interpolation errors. In a time step, the calculation is carried out on all levels, and the updated data on a fine level are averaged onto the underlying coarser one. For a given minimum grid spacing, a higher granularity of the coverage (i.e., the prescription of many small AMR boxes) minimizes the grid count but maximizes data communication between boxes, and vice-versa. Assuming the optimal coverage closely follows the interface, the error compared to uniformly refined grid case is minimal due to dominance of controlling physics near the interface. It is also reasonable to estimate that doubling the grid density in three dimensions corresponds to increasing the storage and the computational cost by an order of 2^3 factor instead of a 2^4 factor (three dimensions plus time) for a grid without AMR. This 50% saving in resources is repeated at every new refinement level.

The blocked-structured AMR framework allows easy implementation of special finite differencing schemes on regular rectangular grids. For example, a geometric multi-grid method that accelerates the convergence of the pressure Poisson's solution is compatible with the block-structured AMR. Another benefit of the framework is reflected by its compatibility with Ghost Fluid treatment for pressure jump conditions to achieve stable and fast pressure solution at high density ratios [40, 41]. By constructing Ghost Fluid regions on both sides of the interface, the method explicitly accounts for the discontinuities of properties across interface. Here, the standard finite difference schemes are revised to capture the pressure discontinuity using Ghost Fluid values, which results in additional terms on the right hand side of the discrete linear equations. The resulting symmetric matrix can be quickly solved using standard linear system solvers. Such sharp interface treatment of pressure jump mitigates the problem of pressure solver divergence that typically occurs at high density ratios.

C. Lagrangian droplet transformation

Although the complex breakup/coalescence of a liquid-gas interface during atomization can be effectively reproduced using direct numerical surface tracking/capturing, the accurate simulation of the evolution of the multitude of very fine droplets that are generated after atomization requires a prohibitively high grid density. In the meanwhile, the small-scale physics of drag and evaporation of individual droplets (neglecting droplet internal flow) in dilute spray regions can be reproduced using established spherical droplet models with reasonable accuracy [47]. A numerical approach has been developed to change the way the liquid phase is described in dilute regions from Eulerian level-set/volume-of-fluid representation to Lagrangian particle representation [38], similar to the algorithms implemented by Herrmann [39] under the framework of the RLSG method. Previously, we have shown that our particular implementation of this Eulerian to Lagrangian droplet transformation [48], when combined with a block-structured AMR technique, provides additional cost-saving benefits, especially when jet column and dense spray region occupy only a small part of the domain. Specifically, when droplets are removed from the Eulerian description, in the region dominated by the droplets the hierarchy of refinement levels quickly reverts to the underlying base level. Thus, the grid refinement remains localized to a small volume around the jet, and the simulation cost is significantly reduced due to a relatively coarse grid far from injection.

The identification of candidate liquid blobs for transformation follows an efficient multi-branch-tree neighbor cell search algorithm [38]. The high efficiency is achieved by recursively searching liquid neighbor cells and simultaneously tagging cell visit history until all the unvisited neighbor cells hit the liquid-gas boundary. The cells belonging to each liquid blob are assigned a unique index and prepared as candidates to be transformed into one Lagrangian particle. During cell search, the blob sizes are obtained by a running-sum of the cell volume. The advantage of computing the running-sum is that it can significantly reduce the cost of searching large-volume blobs by disqualifying such candidate blobs during the early stages of the search. The sphericity, center of mass, average velocity and average temperature of liquid blobs are also computed to be used in later calculations. Note that the adaptive mesh refinement is based on the location of the liquid-gas interface. Therefore small droplets always reside in the finest level box and the identification procedure described above is performed exclusively on the finest level.

The transformation of liquid blobs is based on a number of numerical and physical criteria including blob size, sphericity and local liquid concentration. The volume of a candidate liquid blob is constrained to be less or equal to a critical value,

$$V_L \le V_{cri} = \frac{4}{3}\pi R_{cri}^3 = \frac{4}{3}\pi (m\Delta x)^3 \tag{6}$$

where m is a user-prescribed small integer (m = 4 for the simulation results shown in this paper). If the droplet is small enough, further breakup (referred to as sec-

ondary breakup) rarely occurs due to the high surface tension compared to the aerodynamic force. In the calculations, the Weber number of the Lagrangian particles, defined as $\mathrm{We}_d = \rho_g |\mathbf{u} - \mathbf{u}_d|^2 D/\sigma$, is monitored at each time step, and this diagnostics confirms the absence of the conditions for secondary breakup.

A second criterion is the droplet sphericity, defined as:

$$\alpha = \frac{R_{max}}{\max\left[\Delta x, \left(\frac{3}{4\pi}V_L\right)^{1/3}\right]}, \tag{7}$$

where R_{max} is the maximum distance to center of mass for the liquid structure and V_L is the volume of the liquid structure. Largely deformed liquid blobs have higher probability to experience further break-up, which should be captured in the Eulerian representation. So we ensure that the transformation can occur only when $\alpha \le \alpha_{cri}$, where the critical value is typically $\alpha_{cri} = 4$. If R_{eff} is the effective radius corresponding to the volume V_L, then $R_{max} \le 4\max(\Delta x, R_{eff})$.

We also impose a constraint of maximum local concentration β_{cri} of droplet below which the transformation to the Lagrangian phase can occur. This parameter separates the dense spray region, where droplet interaction can be captured in the Eulerian description, from the dilute spray region, where drop collision is assumed not to happen. The local concentration is defined as ratio of the total liquid volume in an AMR box to the volume of the box. For the cases examined in the following sections, we observed limited sensitivity of the results to variations of this parameter if $\beta_{cri} \sim 0.01$. It has been shown in a previous study [48] that meeting the above combined criteria is critical to avoid erroneous transformation. At the end of the blob identification process, the liquid blob that meets all the transformation criteria is removed from the Eulerian representation by setting the level set ϕ and volume fraction F for the cells there as

$$\varphi = -|\varphi| \quad \text{and} \quad F = 0. \tag{8}$$

While this operation is performed, the volume, center of mass, and velocity for each individual particle are calculated as

$$V_d = \int_d dV, \qquad \mathbf{x}_d = \frac{1}{V_d}\int_d \mathbf{x}\,dV,$$

$$\mathbf{u}_d = \frac{1}{V_d}\int_d \mathbf{u}\,dV, \tag{9}$$

and stored in the list of particles.

The Lagrangian trajectories of the transformed particles are tracked with the base grid flow velocity using a simple discrete particle drag model as

$$\frac{d\mathbf{u}_d}{dt} = F_d(\mathbf{u} - \mathbf{u}_d) \quad \text{and}$$

$$\frac{d\mathbf{x}_d}{dt} = \mathbf{u}_d. \tag{10}$$

The drag for a rigid sphere of diameter D is calculated as

$$F_d = \frac{18\mu_g}{\rho_l D^2}\frac{C_D \mathrm{Re}_d}{24}, \tag{11}$$

with drag coefficient $C_D = 0.424$ for $\mathrm{Re}_d = \rho_g |\mathbf{u} - \mathbf{u}_d| D/\mu_g > 1000$ and

$$C_D = \frac{24}{\mathrm{Re}_d}\left(1 + \frac{1}{6}\mathrm{Re}_d^{2/3}\right) \tag{12}$$

otherwise. The underlying gas flow velocity $\mathbf{u}$ is obtained by interpolation at the instantaneous droplet location. The Lagrangian droplets exert an equal but opposite drag force on the gas, and a two-way coupled system is considered. Since the cost of tracking Lagrangian particles on the coarse grid is negligible compared to fully resolving the interface using a refined grid, significant savings of computational time can be achieved, as demonstrated in a previous investigation [48].

Results

A. Physical parameters and computational setup

The simulations were configured based on the experiment by Sallam et al. [1] to measure the near-field characteristics of non-turbulent water jet in cross flowing air at ambient conditions. The detailed material properties and conditions are listed in Table 1 and 2 respectively. At a fixed momentum flux ratio (q=88.2), the gaseous Weber number is varied from 10 to 160, covering a range of breakup regimes [1, 10] (We=10 bag breakup, We=40 multimode breakup, We=160 shear breakup). Note that the density ratio for water-air system at ambient condition is λ_ρ=845, much higher than what has been simulated by others [44-46].

ρ_l	μ_l	ρ_g	μ_g	λ_ρ	λ_μ	σ
997	0.000894	1.18	0.0000186	845	48	0.0708

Table 1. Material properties in the simulations.

Cases	U_l	U_g	q	We_g	Re_l	Reg
1	8.9	27.4	88.2	10	7896	1391
2	17.7	54.8	88.2	40	15791	2781
3	35.4	109.6	88.2	160	31583	5562

Table 2. Conditions of the simulations.

In the simulations, the coordinate system has the *x*-axis in the crossflow direction and the *z*-axis in the direction of liquid injection. The computational domain is a box of 3.0 cm × 2.0 cm × 5.0 cm. The jet orifice is located at 0.2 cm downstream of domain (0.2, 1.0, 0.0) with a diameter of d_0=0.8 cm. Impermeability and no-slip boundary conditions are imposed at the $z = 0$ plane, except at the jet orifice. Velocity inflow is imposed at the inlet boundary located at $x = 0$ cm and at the jet orifice. Outflow boundary conditions are imposed on the remaining boundary planes. The time stepping of the simulation is defined by two criteria: CFL criterion and surface tension criterion.

$$\Delta t < \min_{i,j}\left(\frac{1}{2}\frac{\Delta x}{\left|\mathbf{u}^n\right|}, \frac{1}{2}\sqrt{\frac{\rho_l}{8\pi\sigma}}\Delta x^{3/2}\right)$$

The simulation starts from the instant when the jet is injected into a uniform gaseous crossflow. The simulations reach full penetration within 10,000 simulation steps (20ms in physical time). A snapshot when the liquid jet reaches full penetration is shown in Fig. 1.

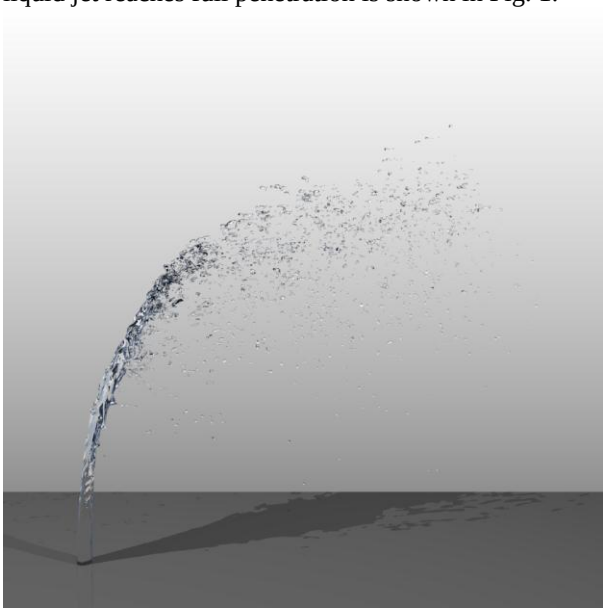

Figure 1. Snapshot of the simulation of liquid jet in crossflow**.**

In the actual experiment [1], in order to suppress the effects of inlet turbulence and to independently investigate the interaction of non-turbulent liquid jet and gaseous flow, a shock-tube and a subsonic wind tunnel were used to generate uniform gas cross flow at high and low speed respectively, together with a sharp edge super-cavitating nozzle to achieve non-turbulent liquid jet out of injection orifice. In our simulation, this is emulated using plug-flow profiles for both the liquid and gas inlets. Fig. 2 demonstrates the simulation of liquid jet penetrating into the gas phase without crossflow interactions. As also shown by Sallam et al. [1] using actual experiment of straight jet penetration (We_g=0), the absence of liquid inlet turbulence suppresses the development of surface waves on the jet column and the jet can penetrate long without significant disturbances on its round surface. This indicates the atomization physics is solely controlled by the aerodynamic forces of the crossflow. Such configurations in both experiment and simulation help simplifying the analyses and achieving better understanding of process.

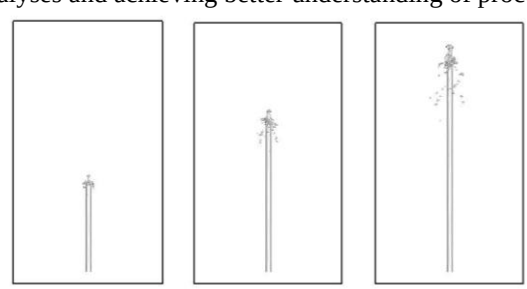

(a) **(b)** **(c)**

Figure 2. Simulation of non-turbulent liquid jet without cross flow: (a) t=0.8ms (b) t=1.4ms (c) t=2ms.

The grid size is selected to be Δx = 39μm for all simulations. Based on Kolmogorov turbulence cascade theory, the grid size required to resolve the smallest dissipative scales is $\Delta x \sim L^{1/4}(\nu/U)^{3/4}$, where L and U are the characteristic integral length scale and velocity scale respectively. For the cases considered in this study, the size can be as small as 0.3μm, as shown in Table 3. While simulating such high resolution cases is

Cases	U_l	U_g	L_l	L_g	Δx_l	Δx_g
1	8.9	27.4	0.0008	0.035	9.51e-7	9.48e-6
2	17.7	54.8	0.0008	0.035	5.68e-7	5.64e-6
3	35.4	109.6	0.0008	0.035	3.37e-7	3.35e-6

Table 3. Grid size estimation based on Kolmogorov turbulent cascade theory.

Simulation type	UG	AMR	AMR-DRP
Grid resolution	$512 \cdot 384 \cdot 896$	$64 \cdot 48 \cdot 112$ (3 level)	$64 \cdot 48 \cdot 112$ (3 level)
Grid count	176.2 M	7.1 M (steady-state)	5.5 M (steady-state)
Cost of 10^4 steps	13.8 days (2016 cores)	20.8 days (24 cores)	14.7 days (24 cores)

Table 4. Grid count and cost for three types of simulations.

beyond current computing capability, it should also be noted that for the cases with suppressed inlet turbulence, the physically relevant flows are controlled by the multiphase interactions and interfacial instabilities, not described by Kolmogorov theory. Therefore, in the current study, the selection of grid size is based on the minimum diameter of ligaments ($d^l_{min} = 64\mu m$) droplets ($d^p_{min} = 77\mu m$) observed in the experiments [1]. The grid resolution here is selected to be smaller than the ligament or droplet size to sufficiently capture the breakup process. Note that actual pinch-off occurs at spatial and temporal scales that are infinitesimally small and a sub-grid model based on micro-scale physics should be included to avoid the singularity in the continuum formulation [49]. As also pointed out by Herrmann [44], the volume error induced by numerical topological change is on the order of grid size and therefore neglected in current study.

As shown in Fig. 3, three types of simulations are performed. The uniform grid simulation (to be referred as UG in subsequent sections) which has the finest grid spread over the whole domain provides the most accurate solution by resolving liquid atomization processes and the gas flow well. The simulations were performed using over 2000 cores on the Titan supercomputer of the Oak Ridge Leadership Computing Facility (OLCF) at Oak Ridge National Laboratory. Simulations that coarsen the gas phase solution using AMR (to be referred as AMR) and those that employ additional coarsening via the introduction of Lagrangian droplets (to be referred as AMR-DRP) were performed using 24 cores each. It is observed in Table 4 that, indeed, AMR and droplet transformation do significantly reduce the grid-count and simulation cost. The 13.8 days UG computation using 2016 cores translates to at least 3.2 years if using 24 cores assuming no memory limit for the machine. The reason for the AMR and AMR-DRP cost difference being small here is that the simulation domain is created to be compact around the liquid jet in order to minimize the grid-count for the UG simulation. The grid-count reduction due to droplet transformation is small (5.5M for AMR-DRP vs. 7.1M for AMR). For cases with much larger domain and larger proportion occupied by dilute spray, the AMR-DRP simulation would provide even more cost advantage. The accuracy of using AMR and AMR-DRP will be evaluated in later sections when the simulation results are compared with the experimental data.

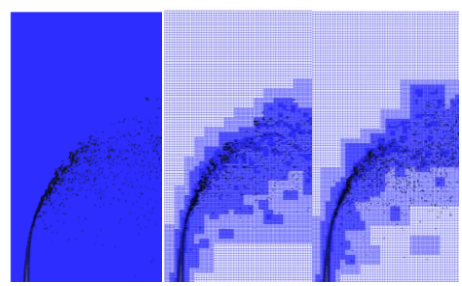

(a) **(b)** **(c)**

Figure 3. Grid configuration for three types of simulations: (a) Uniform-grid (UG), (b) AMR, (c) AMR+droplets (AMR-DRP)

B. Qualitative features of jet atomization and flow

In Fig. 4, the qualitative features of a typical atomization processes are illustrated by the steady-state snapshots of liquid surface and droplets distributed in space at an intermediate Weber number (Case 2, We=40). The images were obtained from the UG simulation performed using OLCF Titan. Fig. 4(a) qualitatively compares well with the two-dimensional side images in Ref. [1] while Fig. 4(b) and (c) provide views that were not obtained in the experimental study. As the jet penetrates into the crossflow, it bends towards the direction of crossflow stream. Due to the pressure difference at the windward and leeward of the column caused by column blockage, the jet also widens in the transverse direction (Fig. 4(b)). For the lower part of the jet, the windward side of the column is mostly orthogonal to the crossflow. Waves form on the lower column surface and the traveling of waves upward along the moving jet surface

is fastest at the mid-plane and slowed down close to the edge of column due to the transverse stretching of the column. As a result, a "Λ" shape wave structure forms on the surface (Fig. 4(b)). For the higher part of the jet, the column bends and the propagation of waves is more inclined with the crossflow direction. Finally the wave growth becomes three-dimensional and sufficiently strong to fragment the jet column into ligaments/large drops (Fig. 4(e)) that further break up into smaller droplets (Fig. 4(f)). On the edge of the jet column, small droplets are also preferentially stripped from the edge at the peak of surface waves due to high shear (Fig. 4(d)). It is noted that the ligaments maintain a state of being stretched for some traveling distance (Fig. 4(d)(e)) before being further fragmented into smaller droplets or relaxed into larger droplets of nearly spherical shape based on local shear conditions. The resulting droplets of different sizes continue to interact with the cross flow, travel downstream and mix with the gas phase.

The instantaneous snapshots of flow pressure, velocity magnitude and vorticity magnitude in different planes are displayed in Fig. 5. Due to the aerodynamic blockage of liquid jet, a high pressure zone is formed on the windward side of the jet and a low pressure wake region is formed on the leeward side of the jet (Fig. 5(a)-(c)). Compared to the upstream cross flow velocity 54.8 m/s, the velocity magnitude is significantly increased (~70 m/s) outside the wake and decreased inside the wake (~10 m/s) (Fig. 5(e)). The liquid jet acts as a bluff body, originating a shear layer at the edge of the jet column and the thickness of the layer grows downstream of the jet (Fig. 5(f)). The formation of large-scale vortex street is also observed in Fig. 5(f). Due to the upward motion of the jet, the wake region is tilted upwards and flow acceleration is observed in a lower region behind the wake (Fig. 5(d)). The introduction of velocity difference and shear layer due to the presence of liquid jet leads to significant flow perturbation as shown in vorticity plot in Fig. 5(g)-(i). The shear layer originated at the liquid-gas interface generates small-scale vortices with high vorticity magnitude (Fig. 5(g)-(h)). As the vortices are transported downstream, their length scale increases as shown by the increased size of flow structures (Fig. 5(d)(h), but their magnitude decreases (Fig. 5(g)(i)). Properly simulating such vortical flow structures is critical for predicting downstream droplet-flow mixing and fuel distribution.

Note that the observations above are qualitative and based on instantaneous snapshots of the liquid column, droplets and flow structures. Some processes such as column fragmentation may be dynamically changing locations. Therefore statistically averaged results over a number of snapshots will be presented next for meaningful quantitative comparison with experimental data.

C. Effects of Weber number on column features and quantitative validation with experiment

The multiphase breakup is controlled by the competition between surface tension and flow forces at the liquid-gas interface. At high gas flow Reynolds number in our study (Table 2), the effects of fluid viscosity are negligible and the Weber number that represents the ratio of inertia to surface tension plays a critical role determining the mechanisms of breakup. According to Sallam and co-workers [1], the breakup of liquid jet in cross flow can be categorized into different regimes (column, bag, multimode, and shear breakup) based on the Weber number, similar to the secondary breakup of drops subjected to shock wave disturbance. Based on Fig. 2 in REF [1], simulations have been performed at three conditions (shown in Table 2) representative of different breakup regimes: case1, We=10, bag breakup; case 2, We=40, multimode breakup; case 3, We=160, shear breakup.

The snapshots of the simulated jet breakup at different conditions are compared in Fig. 6. Compared with the multimode case at We=40, the We=10 case shows a longer wave length along the column (Fig. 6(d)(e)). The amplitude of wave also increases more for We=10 than We=40 as the waves travel along the column. Due to the stronger surface tension relative to aerodynamic force at We=10, much fewer droplets are stripped off the column at the lower part of the jet and breakup mostly occurs at the upper part (Fig. 6(a)(b)). The strong surface waves finally change into concave liquid structures thinning in the middle and thick ligaments continuously elongating at the edges (Fig. 6(d)). The "bags" observed in the experiment [1] represent the infinitesimal liquid membrane of the concave structures before breakup, which cannot be resolved by the grid resolution in the current simulation. However, the processes towards bag breakup are still captured by the simulation with two thick ligaments at the edge formed and breaking up after being elongated. It is observed that larger ligaments and droplets are generated at the upper part of the We=10 case than the We=40 case. The validation of droplets formation will be provided in the next section. Due to the column being sustained contiguous longer at We=10 and the larger Stokes number (the ratio of droplet relaxation time to flow characteristic time) for the larger droplets at We=10, the spray shows a higher penetration. The large ligaments/droplets travel along a straight trajectory and form a sharp angle for the We=10 case in Fig. 6(d) and (g). Overall, the droplet size and distribution are significantly different between the two We cases in Fig. 6(a) and (b), (c) and (d), (g) and (h). Compared with the multimode case at We=40, the shear breakup case at We=160 shows stronger disturbance on the column surface (Fig. 6(f)). Due to stronger aerodynamic shear at We=160, the upper part of the liquid column breaks

up earlier and the penetration of the jet is slight less compared to the case of We=40. The stripping of droplets at the column edge occurs at similar locations but the spread of droplets shows slight difference. The above conclusions regarding spray penetrations and droplet spreading are confirmed in Fig. 7 for the time averaged liquid column and droplets at different conditions. Such averaged pictures resemble more the experimentally obtained pictures usually obtained at longer exposure time than the atomization time scale.

A quantitative comparison of the near-field jet column features with measurements from Sallam et al.[1] is presented in Fig. 8. The near-field column properties including surface wavelength, breakup onset location, column deformation at onset of breakup, column fragmentation location, and column trajectory are obtained by averaging data obtained over a long period after the jet has reached full penetration steady-state. The means are computed and plotted in comparison with the experimentally calibrated correlations. The cartoon inset plots in Fig. 8 explain the properties compared. The color inset plots are used to explain our approach to extract data from simulation results. The standard deviations of the data are listed in Table 5.

Fig. 8(a) compares the surface wavelength predicted by simulations and measured in experiments. The presence of travelling waves is identified by a Proper Orthogonal Decomposition (POD) analysis [50] that was developed to analyze the dynamics of liquid jet atomization processes. The results for the three cases are shown in Fig. 9. By analyzing a time series of images as in the first column in Fig. 9, we are able to extract the first two dominant POD modes that contain most of the energy in the frequency spectrum. For We=10 and We=40, the two modes shown in the second and third column clearly show wave structures with a 90 degree phase shift, which is an indication of the presence of travelling waves. For the case of We=160, the wave structure cannot be observed clearly due to a three-dimensionally perturbed column surface in Fig. 9(g). The wavelength is computed by dividing the length of a certain segment by the number of waves within the segment. The data in Fig. 8(a) shows that the simulation at We=40 predict very well the wavelengths on the column, which match well with the experimental correlation [1]

$$\lambda_s / d_0 = 3.4 We^{-0.45}. \tag{13}$$

The prediction for the We=10 case also compares reasonably well with the correlation while the prediction for the We=160 case cannot be obtained due to the absence of two-dimensional traveling waves in the current simulation.

Fig. 8 (b) and (c) compare the location for the onset of breakup and the column deformation in crossflow direction at this location. The location is identified by recording the location of first ligaments that pinch off to form droplets. The deformation is measured as the distance between windward and leeward surface in a plane cut through the onset location (Fig. 8(c) inset). It is observed that the onset location and column deformation at We=40 compare well with experimental correlations [1]

$$d_0 / d_j = \begin{cases} 2 & 4 < We_g < 30 \\ 12 We_g^{-0.53} & 30 \le We_g \le 110 \\ 1 & We_g > 110 \end{cases}. \tag{14}$$

$$t_i / t_v = 0.0004 \left(\lambda_\mu / We_g \right). \tag{15}$$

The comparison is good for We=160 case as well while slight discrepancy is observed for the We=10 case. One possible reason for the discrepancy is the inability of capturing “bags” in the simulation that leads to the error in predicting of the drag imposed on the jet, the bending of the jet and therefore the deformation that is related to the bending.

In Fig. 8(d), the locations of column breakup are compared. The breakup points are identified by combining two different views as shown in the inset of Fig. 8(d). The experimentally measure column breakup location is

$$x_b / d_0 = 8.0, \tag{16}$$

$$y_b / \left(d_0 q^{0.5} \right) = 2.5. \tag{17}$$

Searching the breakup location using only one view, as has been done in most experimental studies [1, 8], may cause mis-identification due to the obtrusion by neighboring liquid structure. As a result, in most cases both x and y breakup locations obtained by our approach are slightly smaller than those reported experimentally.

In Fig. 8, the predictions using different numerical configurations (UG, AMR, AMP-DRP) are compared. Compared with the UG case, the AMR and AMR-DRP cases have reduced resolution in gas dominated regions. Although the flow features away from the jet column are expected to be different due to different grid resolutions (the small-scale flow turbulence being suppressed by numerical dissipation of coarser grid), the small scale processes on the column surface is less affected by the upstream gas flow (non-turbulent in the current study) and the zone enclosing the jet column are resolved to the same level of accuracy. The prediction of the overall deflection and penetration of the jet column matches well with the data for the We=40 case in Fig. 8(d), irrespective of whether the AMR is adopted or not. Also the small scale process occurring on the surface such as surface waves, jet deformation and stripping is well predicted using AMR (Fig. 8(a)-(c)) due to the fact the liquid structures resulting from interfacial instabilities and breakup are well captured by the refined mesh. The AMR-DRP case compares well with the AMR case for the near-field column features be-

cause the introduction of Lagrangian droplets occurs away from the column surface. As shown in Table 5, the standard deviations of the data are mostly around 10%, consistent with the 10% uncertainty for most correlations reported by the experimental study [1]. The slightly higher deviation in surface wavelength for AMR and AMR-DPR cases can be attributed to the numerical error in gas phase solutions. Longer simulation time and more data sampling may help reduce the deviations in the data. In summary, the liquid breakup details are quantitatively captured by the simulations using the AMR configuration, which establish the equivalence between the two approaches in predicting near-field details. It is expected the reduced resolution in the gas dominated regions will lead to numerical dissipation and the impact of grids on downstream droplet transport will be the focus of future work.

D. Effects of Weber number on droplet formation and quantitative validation with experiment

The key physics in liquid jet primary atomization lies in the process of liquid column breaking up into ligaments then droplets. In this section, the formation of droplets is quantitatively studied by recording the events right after liquid structures are broken off the jet column and fragmented into small and spherical blobs. The events are numerically captured using the Lagrangian transformation algorithms when the candidate liquid structures away from the jet column satisfy the transformation criteria introduced in section II.C. Droplet data including size, location, velocity and instant of transformation are collected for 10 ms in physical time after the jet reaches full penetration steady state. Over 20,000 droplets are collected for each case. The collected droplets are spatially distributed near the jet column as shown in Fig. 10. The droplet size and velocity are shown in Fig. 10(a) and (b) respectively. It is noted that the droplet size and velocity along the column surface were also measured by Sallam and reported in Ref. [1]. However, the detailed steps of identifying droplets and measure their sizes using two-dimensional shadowgraph images are not reported. Whether the identified droplets will experience secondary breakup or not was not reported in Ref. [1]. Therefore the size parameter ("m" in Eq.(6)) is relaxed to a sufficiently large number m=10 ($R_{cri} = m\,\Delta x = 390\,\mu m$) in our simulations to capture all the blobs possibly encountered in the experimental measurements. Next, we will present in more detail such droplet data and compare with the measurements when possible.

The size distributions of droplets generated along the liquid column surface are shown in Fig. 11 with data obtained at different We compared in three columns. The detailed size probability distributions (number density) at different z locations are also plotted and compared. As observed in section III.C, most droplets are generated at the upper part of the column for the case of We=10 (Fig.4(a)), compared to the other two cases. Slightly more droplets are generated at the lower part of the column for the case of We=160 (Fig. 11(c)) than We=40 (Fig.11(b)). The experimentally obtained correlation is

$$d_p/d_0 = \begin{cases} 4.32\left[(\nu_L z)/(v_j d_0^2)\right]^{0.5} & (\nu_L z)/(v_j d_0^2) < 0.001 \\ 0.132 & (\nu_L z)/(v_j d_0^2) \geq 0.001 \end{cases}. \tag{18}$$

The correlation curve falls within the data collected in the simulation. The detailed size probability distribution at three different z locations are shown in the bar-chart (d)-(l). The peak sizes are mostly around 100-120 μm at all locations for all We, close to the value of 106 μm given in the correlation. The smallest droplet sizes observed are 40μm due to a grid resolution of Δx=39μm in the simulations. Even smaller droplets may be present in the actual process but are not captured by current simulations as well as measurements. For the case of We=10, the largest droplet size observed increases from 240 μm to more than 400 μm from z/d_0=15 to z/d_0=25 due to the breakup transition from surface stripping to the rupture of thick ligaments enclosing the "bag" (concave liquid membrane). For the cases of We=40 and 160, the largest droplet size first increases then decreases. The increase can be explained by the formation of large droplets due to column breakup. The decrease is due to reduced penetration and depletion of droplets. As We increases from 10 to 40, the largest droplet size increases at z/d_0=15, remains mostly unchanged at z/d_0=20, decreases at z/d_0=25.

The distributions of three velocity components of the droplets generated along the liquid surface are plotted in Fig. 12 with data obtained for different We compared in three columns. The detailed velocity probability distributions at z/d_0=20 are also plotted and compared. As studied in Ref. [1], the droplet U velocity component is scaled by the combination of cross flow gas velocity and density ratio

$$u_p/u_L = u_p(\rho_L/\rho_G)^{0.5}/u_\infty \tag{19}$$

to reflect the scaling of momentum exchange between liquid and gas. The V and W velocity components are scaled by the liquid injection velocity w_j. Experimental correlations

$$u_p/u_L = 6.7 \tag{20}$$

$$w_p/w_j = 0.7 \tag{21}$$

were obtained for the U and W velocity components only and the curves fall within the data collected in the simulation. The transverse component V of the velocity field was not measured in the experiment due to the use of two-dimensional image analysis. The detailed velocity probability distribution at z/d_0=20 are shown in the

bar-chart (d)-(l). The distributions for the U component are similar for all three conditions, indicating that the droplet velocity scales with the gas velocity in the cross flow direction. The peak value around 12 is larger than the value of 6.7 in the correlation. The discrepancy might be due to the large uncertainties in determining the droplet velocity using two-dimensional images. The distributions for the W component are also similar for all three conditions, indicating that the droplet upward velocity scales with the liquid injection velocity. The peak value of around 0.5-0.6 is in reasonable agreement with the value of 0.7 in the correlation. An important feature discovered by the simulation is the V component distributions that were not reported in Ref [1]. It is observed that V velocity peaks at very small values for all conditions, indicating the majority of the droplets do not have much transverse motion. However, the distribution shifts towards lower velocity range as We increases. Since the droplet sizes are similar for all three conditions (Fig. 11(g)-(i)), the reduced V velocity is the result of less widening and less blockage effect at higher We, as observed in Fig. 6(d)-(f).

In addition to droplet size and velocity, an additional rate quantity, droplet formation rate, needs to be extracted in order to completely describe the process of droplets formation. The quantity represents the flux of the liquid leaving the contiguous jet column and becoming discrete droplets. In Ref. [1], a quantity called droplet formation efficiency is defined as

$$\varepsilon = \dot{m}''_L / \left(\rho_L u_p\right) \tag{22}$$

where $\dot{m}''$ is the droplet formation rate, representing the flux of liquid through a downstream projected area and u_p is the droplet velocity component in the crossflow direction In our simulation, the flux $\dot{m}''$ is computed as

$$\dot{m}''(i) = \frac{\pi \rho_L \sum_j \left(d_p^j\right)^3}{6\Delta t_{sample} A_i}. \tag{23}$$

The droplets generated along the column surface are divided into a number of bins along z direction. The bin size is selected to be d_0.The projected area A_i for the ith bin of droplets is approximated by the area of a rectangular with vertices defined by the maximum/minimum droplet location in the y-z plane. The summation in Eq. (24) is over all the droplets generated within the ith bin. Therefore, the efficiency is computed as

$$\varepsilon = \frac{N\pi \sum_j \left(d_p^j\right)^3}{6\Delta t_{sample} A_i \sum_j u_p}. \tag{24}$$

Fig. 13 shows the computed efficiency along column surface locations in the z directions at different We. At all three conditions, the efficiency first increases due to the enhanced liquid fragmentation by column breakup at upper part of the jet compared to the surface stripping at the lower part of the jet. It then decreases beyond the column breakup point $z/z_b=1$, where z_b is the column breakup location in the z direction. Compared with the case of We=40 and We=160, the case of We=10 has lower breakup efficiency at the lower part of jet and slightly higher efficiency at the higher part, mostly due to the dominant role of column breakup compared to surface stripping at We=10. The cases of We=40 and We=160 have very similar breakup efficiency. Although the curves largely deviate from the experimental correlation developed by Sallam [1]

$$\varepsilon = 6.89 \times 10^{-4} \exp\left(5.43 z / z_b\right) \tag{25}$$

for the shear breakup regime (Solid line in Fig. 13), the slope of the efficiency increase in the two simulations is comparable with the correlation. Since the definition of A_i in deriving Eq. (25) is not provided in Ref. [1], the discrepancy can be possibly explained by the differences in defining A_i, which leads to a shift of curves without slope change in log scale. Therefore we conclude that the simulated rate change along the column surface compares well with results obtained from Sallam's experiments.

Summary

Liquid jet atomization in crossflow at high density ratio has been studied using a high-fidelity CLSVOF and Lagrangian droplets approach for simulating complex multiphase flows. High performance computing facilities at Oakridge National Laboratory of the US Department of Energy were leveraged to perform the high resolution, high cost simulations. The simulations successfully capture the near-field details of primary liquid jet atomization due to its interaction with crossflowing gas. The effects of gas flow Weber number on the jet column evolution and subsequent droplet formation are explored and the data match the recent near-field experimental measurement using pulsed shadowgraph techniques. It was also shown that Adaptive Mesh Refinement can capture these near-field atomization details at significantly reduced cost.

Acknowledgements

The authors wish to acknowledge the funding support from United Technologies Corporation. They also acknowledge the computer resource and staff support from the Oak Ridge Leadership Computing Facility at Oak Ridge National Laboratory, which is supported by the Office of Science of the Department of Energy under Contract DE-AC05-00OR2272.

Nomenclature

C_D	=	drop drag coefficient
D	=	drop diameter
d_0	=	injector orifice diameter
F	=	volume of fluid function

F_d	=	drag on a drop
N_{step}	=	computational step number
Re	=	Reynolds number
q	=	momentum flux ratio
t	=	time
$\mathbf{u}$	=	velocity
U	=	imposed velocity
V	=	volume
We	=	Weber number
$\mathbf{x}$	=	coordinate
x,	=	coordinate in direction of crossflow
y,	=	coordinate orthogonal to x and z
z,	=	coordinate in direction of liquid injection
Δt	=	time step
Δx	=	grid spacing
λ_μ	=	viscosity ratio
λ_ρ	=	density ratio
μ	=	dynamic viscosity
ρ	=	density
ϕ	=	level set function
σ	=	surface tension

subscripts

d	=	droplet property
F	=	fuel
A	=	air
g	=	gas property
l	=	liquid property
min	=	minimum

superscripts

l	=	ligament property
p	=	particle property
n	=	computational step n

References

1. Sallam, K.A., Aalburg C. and Faeth, G. M., *Breakup of Round Nonturbulent Liquid Jets in Gaseous Crossflow.* AIAA Journal, 2004. **42**(12): p. 2529-2540.
2. Mazallon, J., Dai, Z., and Faeth, G. M., *Primary Breakup of Nonturbulent Round Liquid Jets in Gas Crossflows.* Atomization and Sprays, 1999. **9**(3): p. 291-311.
3. Beale, J.C. and R.D. Reitz, *Modeling spray atomization with the Kelvin-Helmholtz/Rayleigh-Taylor hybrid model.* Atomization and Sprays, 1999. **9**(6): p. 623-650.
4. Kush, E.A., and Schetz, J. A., *Liquid Jet Injection into a Supersonic Flow.* AIAA Journal, 1979. **11**(9): p. 1223-1224.
5. Nejad, A.S., and Schetz, J. A., *Effects of Properties and Locations in the Plume or Droplet Diameter for Injection in a Supersonic Stream.* AIAA Journal, 1983. **21**(7): p. 956-961.
6. Schetz, J.A.a.P., A., *Penetration of a Liquid Jet in Subsonic Airstreams.* AIAA Journal, 1997. **15**(10): p. 1385-1390.
7. Nguyen, T.T., and Karagozian, A. R., *Liquid Fuel Jet in a Subsonic Crossflow.* Journal of Propulsion Power, 1992. **8**(1): p. 21-29.
8. Wu, P.K., Kirkendall, K. A., Fuller, R.P., and Nejad, A. S., *Breakup Processes of Liquid Jets in Subsonic Crossflows.* Journal of Propulsion and Power, 1997. **13**(1): p. 64-73.
9. Hsiang, L.P., and Faeth, G. M., *Near-Limit Drop Deformation and Secondary Breakup.* International Journal of Multiphase Flow, 1992. **18**(5): p. 635-652.
10. Hsiang, L.P., and Faeth, G. M., *Drop Deformation and Breakup Due to Shock Wave and Steady Disturbances.* International Journal of Multiphase Flow, 1995. **21**(4): p. 545-560.
11. Becker, J., and Hassa, C., *Breakup and atomization of a kerosene jet in crossflow at elevated pressure.* Atomization and Sprays, 2002. **11**: p. 49-67.
12. O'Rourke P. J., A., A. A., *The TAB method for numerical calculation of spray droplet breakup.* SAE Technical Paper 1987: p. 872089.
13. Park, J.H., Y. Yoon, and S.S. Hwang, *Improved TAB model for prediction of spray droplet deformation and breakup.* Atomization and Sprays, 2002. **12**(4): p. 387-401.
14. Reitz, R.D. and F.V. Bracco, *MECHANISM OF ATOMIZATION OF A LIQUID JET.* Physics of Fluids, 1982. **25**(10): p. 1730-1742.
15. Reitz, R.D., *Modeling atomization processes in high-pressure vaporizing sprays.* Atomization and Sprays Technology, 1987. **3**: p. 309-337.
16. Madabhushi, R.K., *A model for numerical simulation of breakup of a liquid jet in crossflow.* Atomization and Sprays, 2003. **13**(4): p. 413-424.
17. Jenny, P., D. Roekaerts, and N. Beishuizen, *Modeling of turbulent dilute spray combustion.* Progress in Energy and Combustion Science, 2012. **38**(6): p. 846-887.
18. Chesnel, J., et al., *SUBGRID ANALYSIS OF LIQUID JET ATOMIZATION.* Atomization and Sprays, 2011. **21**(1): p. 41-67.
19. Chesnel, J., et al., *LARGE EDDY SIMULATION OF LIQUID JET ATOMIZATION.* Atomization and Sprays, 2011. **21**(9): p. 711-736.
20. Lebas, R., et al., *Numerical simulation of primary break-up and atomization: DNS and*

modelling study. International Journal of Multiphase Flow, 2009. **35**(3): p. 247-260.

21. Gorokhovski, M.H.a.M., *A Large Eddy Simulation Subgrid Model for Turbulent Phase Interface Dynamics*, in *11th Triennial Conference on Liquid Atomization and Spray Systems*2009: Vail, CO. p. Paper No. ICLASS2009-205.
22. M. Herrmann and M. Gorokhovski. *An outline of an LES subgrid model for liquid/gas phase interface dynamics*. in *Proceedings of the 2008 Summer Program, Center for Turbulence Research*. 2008.
23. Sethian, J.A., Smereka, P., *Level Set Methods for Fluid Interfaces.* Annual Review of Fluid Mechanics 2003. **35**: p. 341-372.
24. Desjardins, O., V. Moureau, and H. Pitsch, *An accurate conservative level set/ghost fluid method for simulating turbulent atomization.* Journal of Computational Physics, 2008. **227**(18): p. 8395-8416.
25. Desjardins, O. and H. Pitsch, *A spectrally refined interface approach for simulating multiphase flows.* Journal of Computational Physics, 2009. **228**(5): p. 1658-1677.
26. Desjardins, O. and H. Pitsch, *DETAILED NUMERICAL INVESTIGATION OF TURBULENT ATOMIZATION OF LIQUID JETS.* Atomization and Sprays, 2010. **20**(4): p. 311-336.
27. Raessi, M. and H. Pitsch, *Consistent mass and momentum transport for simulating incompressible interfacial flows with large density ratios using the level set method.* Computers & Fluids, 2012. **63**: p. 70-81.
28. Scardovelli, R., Zaleski, S., *Direct Numerical Simulation of Free-Surface and Interfacial Flow.* Annual Review of Fluid Mechanics, 2003. **31**: p. 567-603.
29. Tomar, G., et al., *Multiscale simulations of primary atomization.* Computers & Fluids, 2010. **39**(10): p. 1864-1874.
30. Tryggvason, G., Bunner, B., Esmaeeli, A., Juric, D., Al-Rawahi, N., Tauber, W., Han, J., Nas, S., and Jan, Y. J., *A front-tracking method for the computations of multiphase flow.* Journal of Computational Physics 2001. **169**(2): p. 708-759.
31. Unverdi, S.O. and G. Tryggvason, *A FRONT-TRACKING METHOD FOR VISCOUS, INCOMPRESSIBLE, MULTI-FLUID FLOWS.* Journal of Computational Physics, 1992. **100**(1): p. 25-37.
32. Herrmann, M., *A balanced force refined level set grid method for two-phase flows on unstructured flow solver grids.* Journal of Computational Physics, 2008. **227**(4): p. 2674-2706.
33. Himeno, T., Watanabe, T., and Konno, A., *Numerical analysis for propellant management in rocket tanks.* Journal of Propulsion and Power, 2005. **21**(1): p. 76-86.
34. Shinjo, J. and A. Umemura, *Simulation of liquid jet primary breakup: Dynamics of ligament and droplet formation.* International Journal of Multiphase Flow, 2010. **36**(7): p. 513-532.
35. Sussman, M., Smith, K. M., Hussaini, M.Y., Ohta, M., and Zhi-Wei, R., *A sharp interface method for incompressible two-phase flows.* Journal of computational physics, 2007. **221**: p. 469-505.
36. Menard, T., S. Tanguy, and A. Berlemont, *Coupling level set/VOF/ghost fluid methods: Validation and application to 3D simulation of the primary break-up of a liquid jet.* International Journal of Multiphase Flow, 2007. **33**(5): p. 510-524.
37. Cousin, J., et al., *Primary breakup simulation of a liquid jet discharged by a low-pressure compound nozzle.* Computers & Fluids, 2012. **63**: p. 165-173.
38. Arienti. M., X.L., M. C. Soteriou, C. A. Eckett, M. Sussman, R. J. Jensen, *Coupled Level-Set/Volume-of-Fluid Method for Simulation of Injector Atomization*. JOURNAL OF PROPULSION AND POWER, 2013. **29**(1): p. 147-157.
39. Herrmann, M., *A parallel Eulerian interface tracking/Lagrangian point particle multi-scale coupling procedure.* Journal of Computational Physics, 2010. **229**(3): p. 745-759.
40. Kang, M., Fedkiw, R. P. and Liu, X. D., *A Boundary Condition Capturing Method for Multiphase Incompressible Flow.* Journal of Scientific Computing, 2000. **15**(3): p. 323-360.
41. Liu, X.D., Fedkiw, R. P., and Kang, M., *A Boundary Condition Capturing Method for Poisson's Equation on Irregular Domains.* Journal of Computational Physics, 2000. **160**: p. 157-178.
42. Oliger, M.J.B.a.J., *Adaptive mesh refinement for hyperbolic partial differential equations.* Journal of Computational Physics, 1984. **53**: p. 484–512.
43. A.S. Almgren, J.B.B., P. Colella, L.H. Howell, M. Welcome, *A conservative adaptive projection method for the variable density incompressible Navier–Stokes equations.* Journal of Computational Physics, 1998. **142**: p. 1-46.

44. Herrmann, M., *Detailed Numerical Simulations of the Primary Atomization of a Turbulent Liquid Jet in Crossflow.* ASME Journal of Engineering for Gas Turbines and Power, 2010. **132**(6): p. 061506,1-10.
45. Herrmann, M. *The Influence of Density Ratio on the Primary Atomization of a Turbulent Liquid Jet in Crossflow*. in *Proceedings of Combustion Institute*. 2011.
46. M. Herrmann, M.A., and M. Soteriou, *The Impact of Density Ratio on the Liquid Core Dynamics of a Turbulent Liquid Jet Injected into a Crossflow.* ASME Journal of Engineering for Gas Turbines and Power, 2011. **133**(6): p. 061501-9.
47. Sirignano, R.H.R.a.W.A., *An Evaluation of the Point-Source Approximation in Spray Calculations.* Numerical Heat Transfer, 1989. **Part A 16**: p. 37.
48. Li, X., Arienti, M., Soteriou, M. C., and Sussman, M. M., *Towards an Efficient, High-Fidelity Methodology for Liquid Jet Atomization Computations*, in *AIAA Aerospace Sciences Meeting*2010: Orlando, FL. p. AIAA 2010-092407.
49. Arienti, M., Pan, W., Li, X., and Karniadakis, G., *Many-body dissipative particle dynamics simulation of liquid/vapor and liquid/solid interactions.* The Journal of Chemical Physics, 2011. **134**: p. 204114.
50. Arienti, M. and M.C. Soteriou, *Time-resolved proper orthogonal decomposition of liquid jet dynamics.* Physics of Fluids, 2009. **21**(11).
51. Arienti, M., et al., *Modeling Wall Film Formation and Breakup Using an Integrated Interface-Tracking/Discrete-Phase Approach.* Journal of Engineering for Gas Turbines and Power-Transactions of the Asme, 2011. **133**(3).
52 Li, X., and M.C. Soteriou, *High-fidelity simulation of fuel atomization in a realistic swirling flow injector*. Atomization and Sprays, 2013, **23**(11): p. 1049-1078

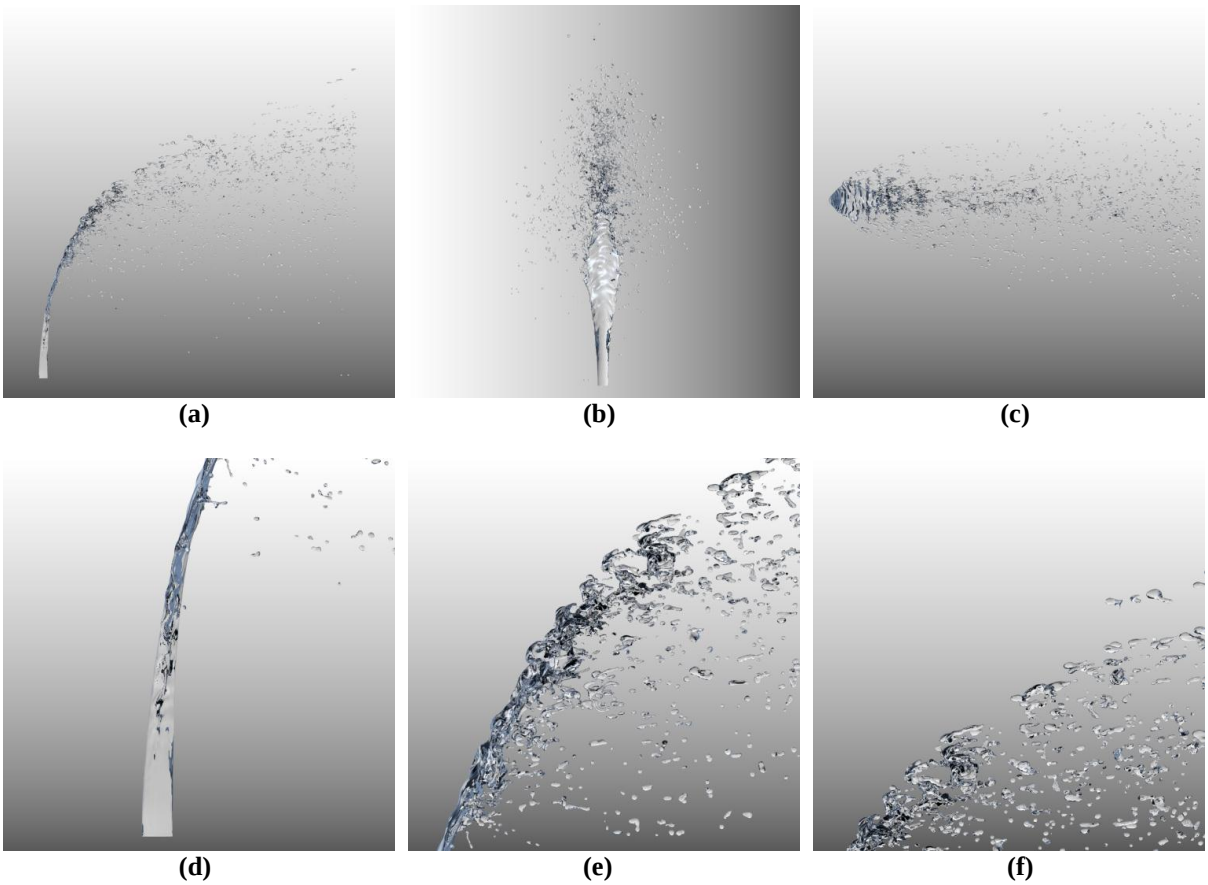

Figure 4. (a)-(c) Jet breakup instantaneous snapshots in different views, (d)-(f) zoomed view of breakup details, We=40.

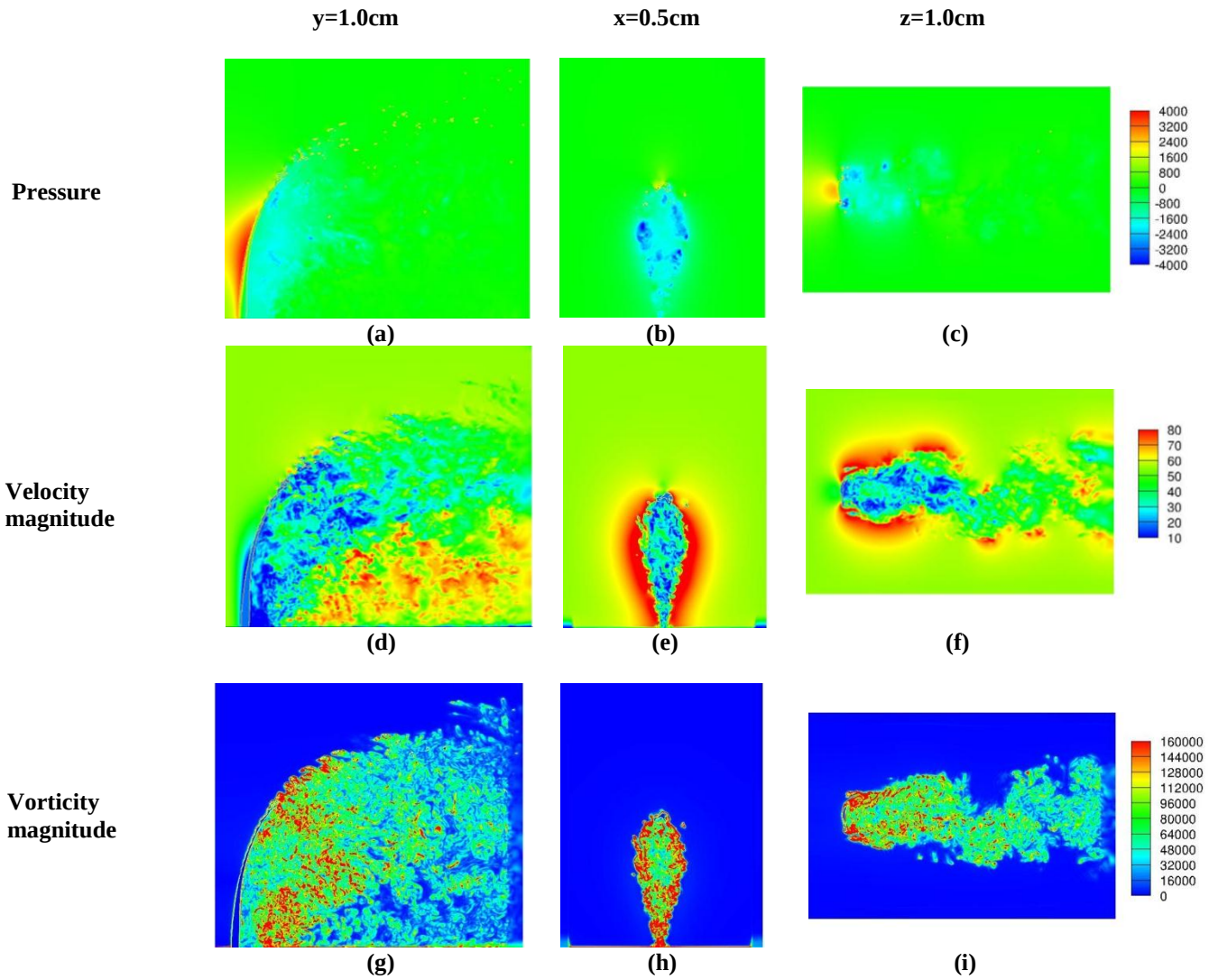

Figure 5. Instantaneous snapshots of pressure, velocity magnitude and vorticity magnitude in different planes, We=40.

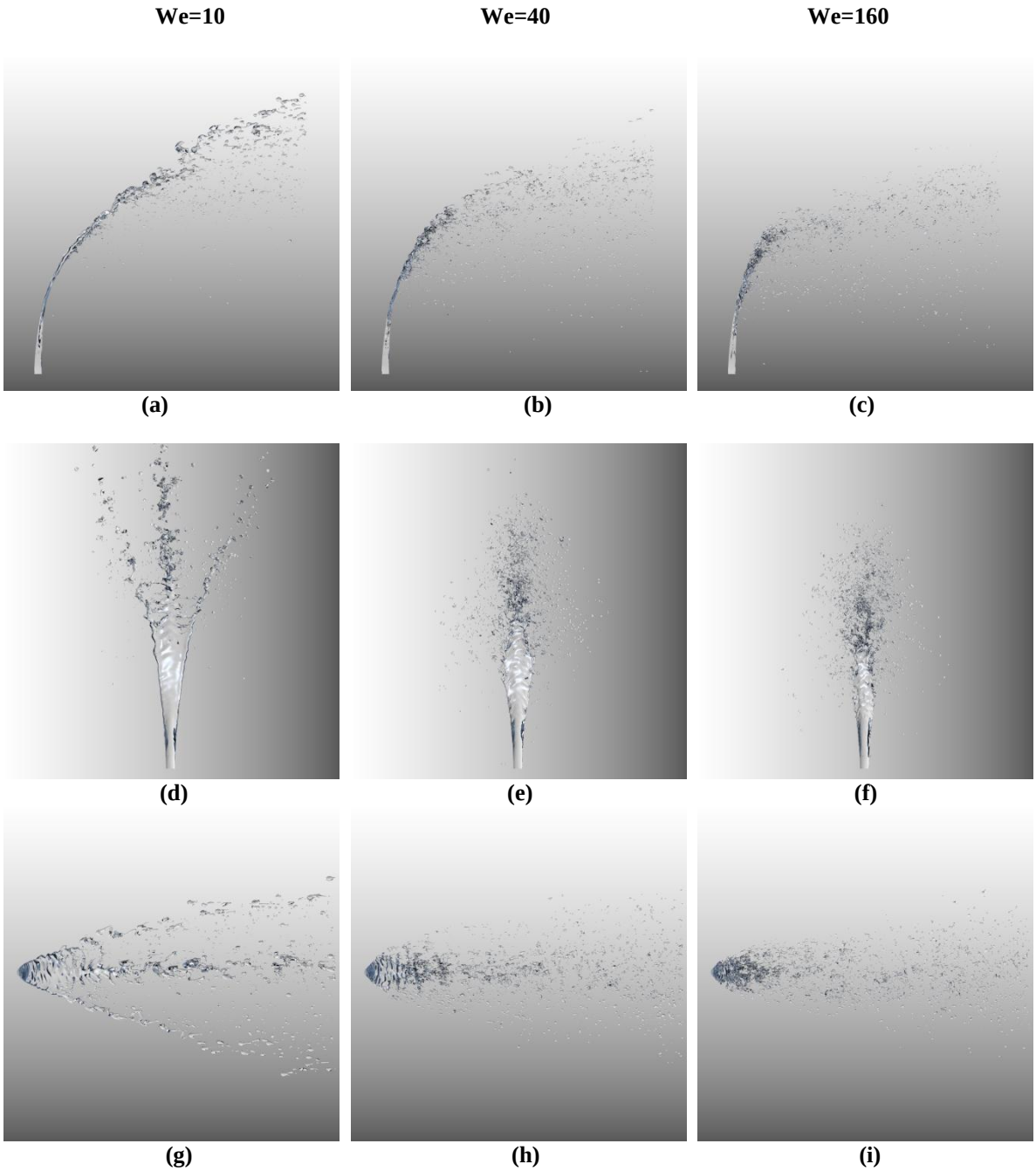

Figure 6. Comparison of instantaneous liquid breakup at different Weber numbers**.**

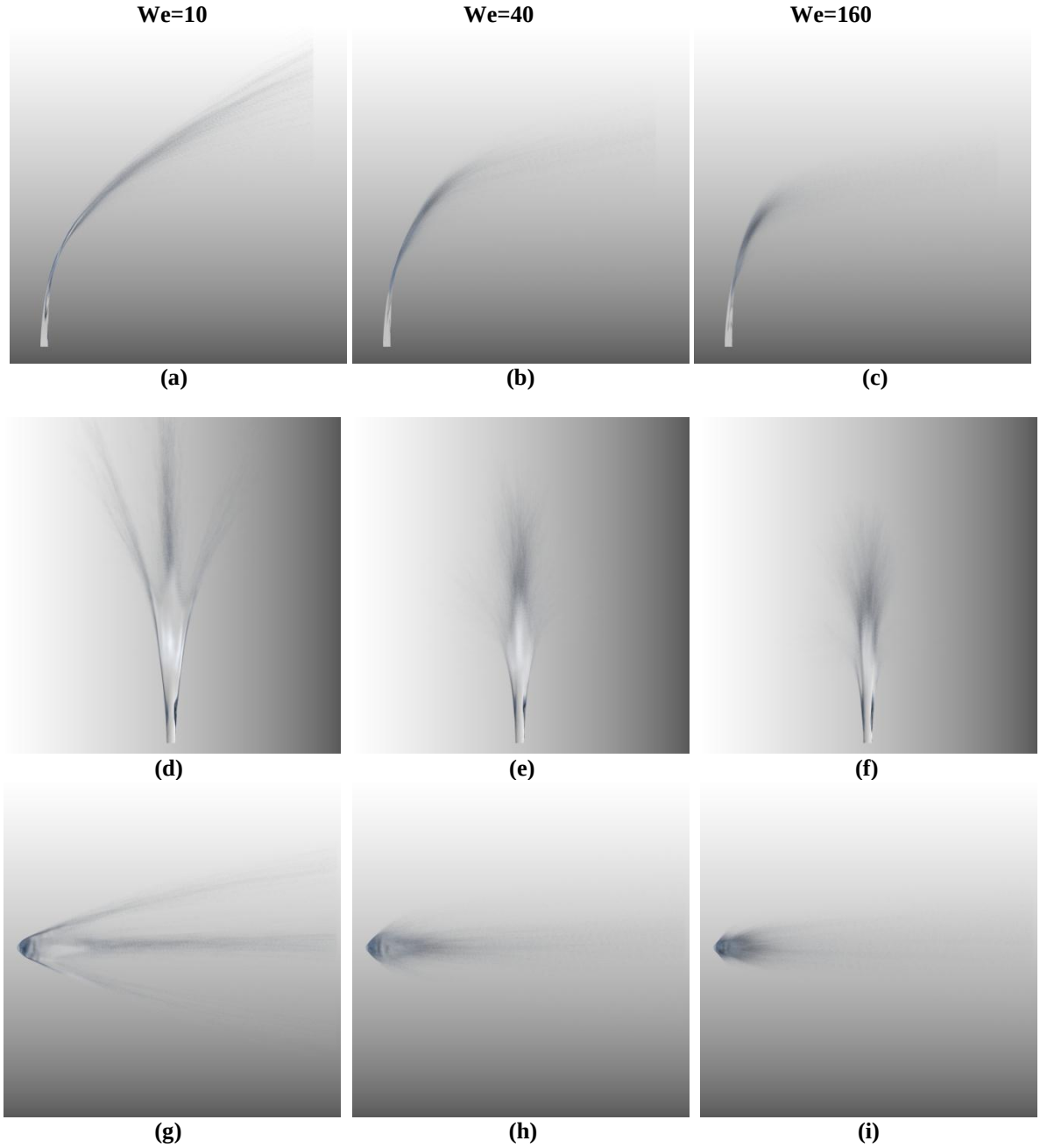

Figure 7. Comparison of averaged liquid surface at different Weber numbers. The time periods for averaging are 1.6ms for We=10, 0.8ms for We=40, and 0.4ms for We=160.

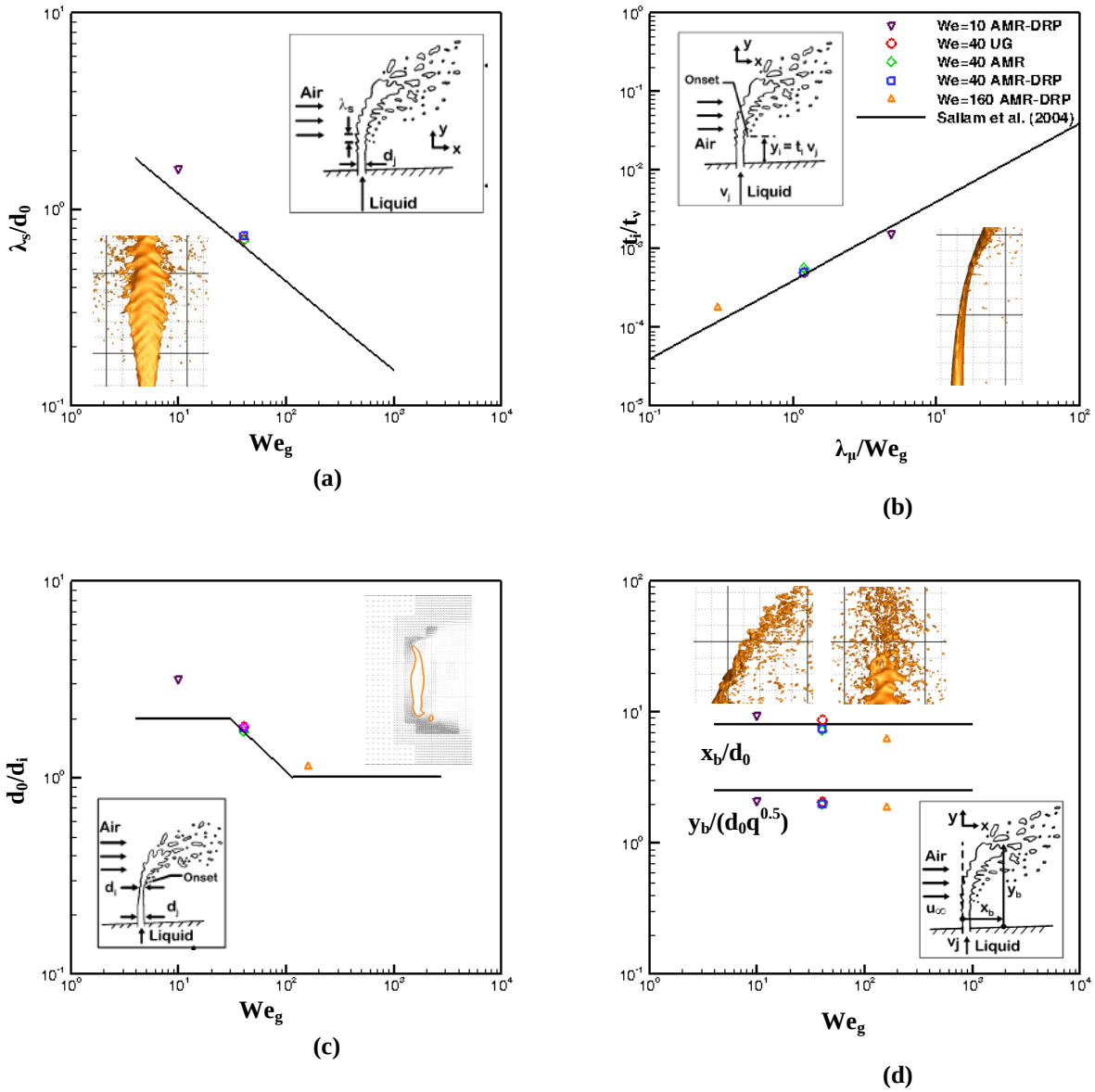

Figure 8. Quantitative comparison of simulated liquid column data with experimental correlations by Sallam et al. [1]: (a) surface wavelength, (b) location at onset of breakup, $\mathbf{t_v = \rho_l d_0^2/\mu_l}$ (c) deformation at onset of breakup and (d) column breakup location. The time periods for averaging are 1.6ms for We=10, 0.8ms for We=40, and 0.4ms for We=160.

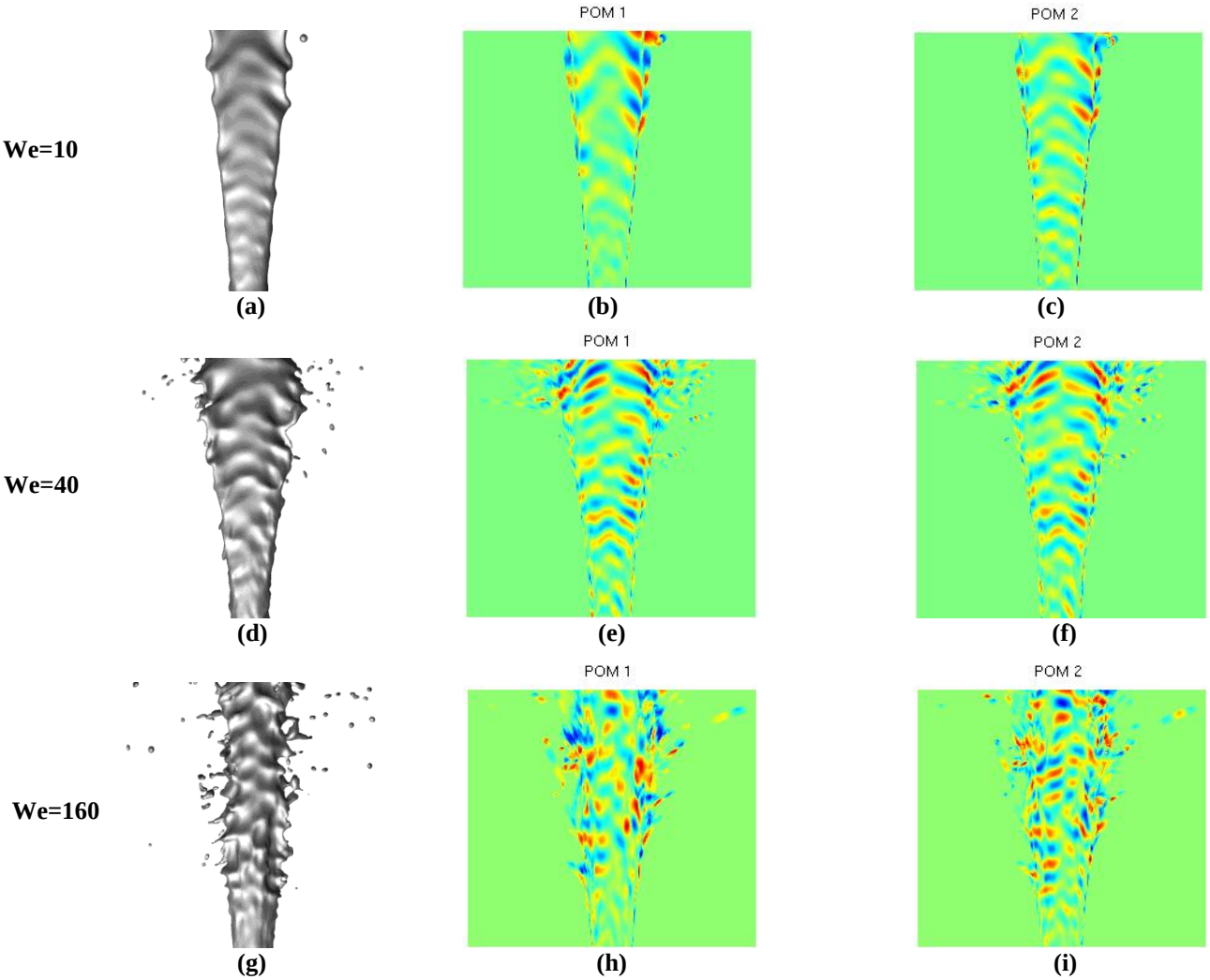

Figure 9. Comparison of liquid column waves details at different Weber numbers. Two dominant modes generated using Proper Orthogonal Decomposition (POD) analysis are also plotted.

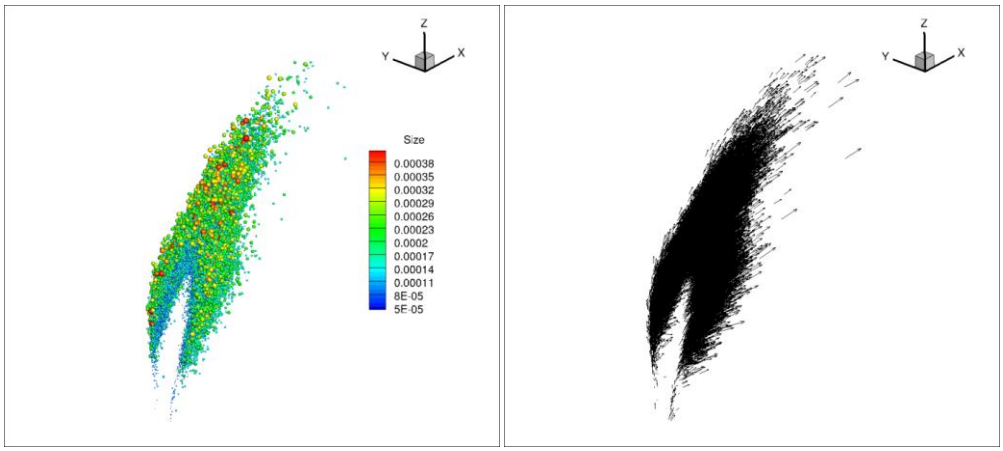

(a) **(b)**

Figure 10. (a) Size and (b) velocity of droplets generated near liquid jet column, We=40.

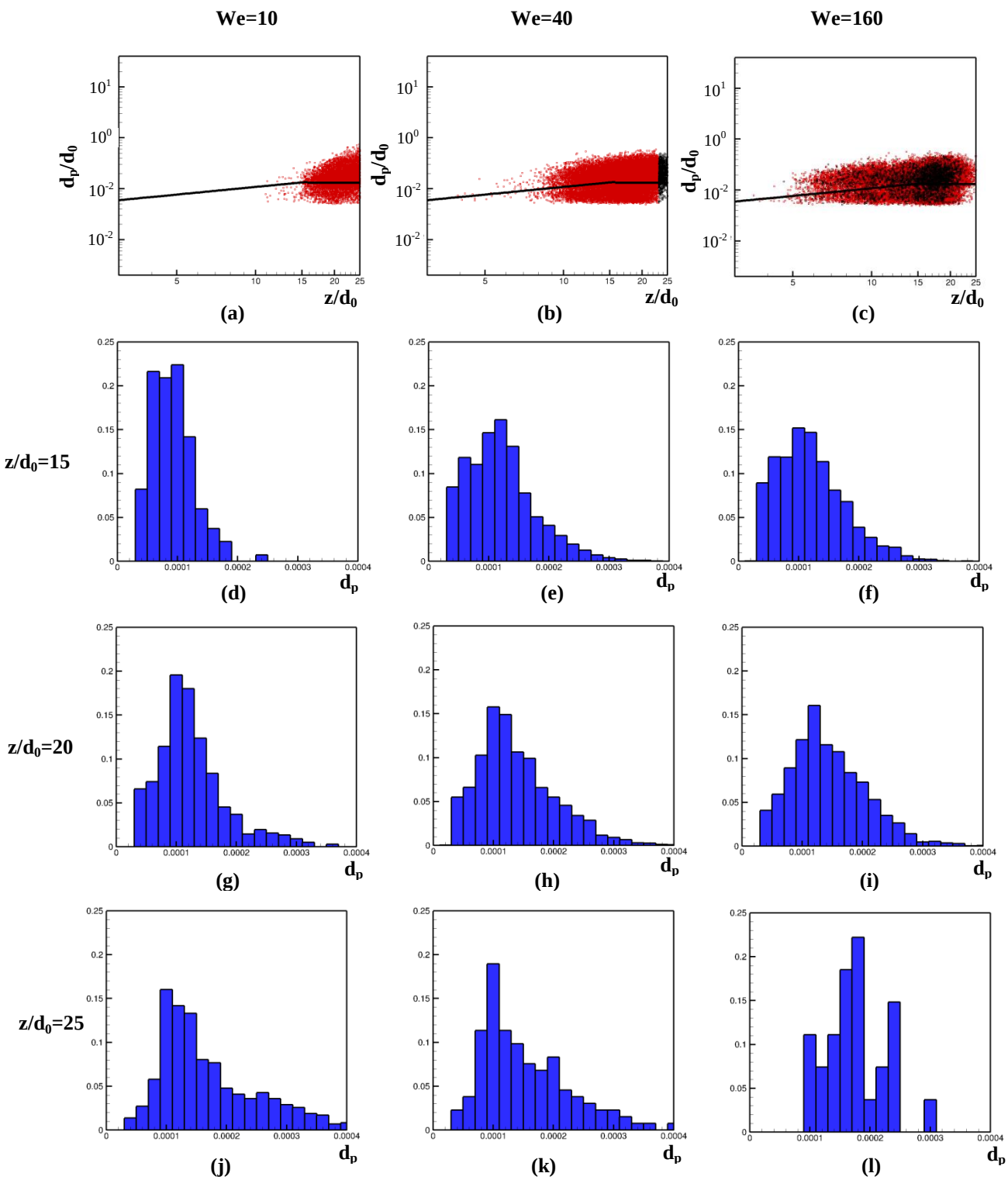

Figure 11. (a)-(c) shows droplet size along z coordinates at different We. Experimental correlation for size (solid line) by Sallam et al. [1] is also shown. (d)-(l) shows corresponding droplet size probability distribution at different z locations. The probability is represented by the droplet number density. The unit for d_p is SI unit "m".

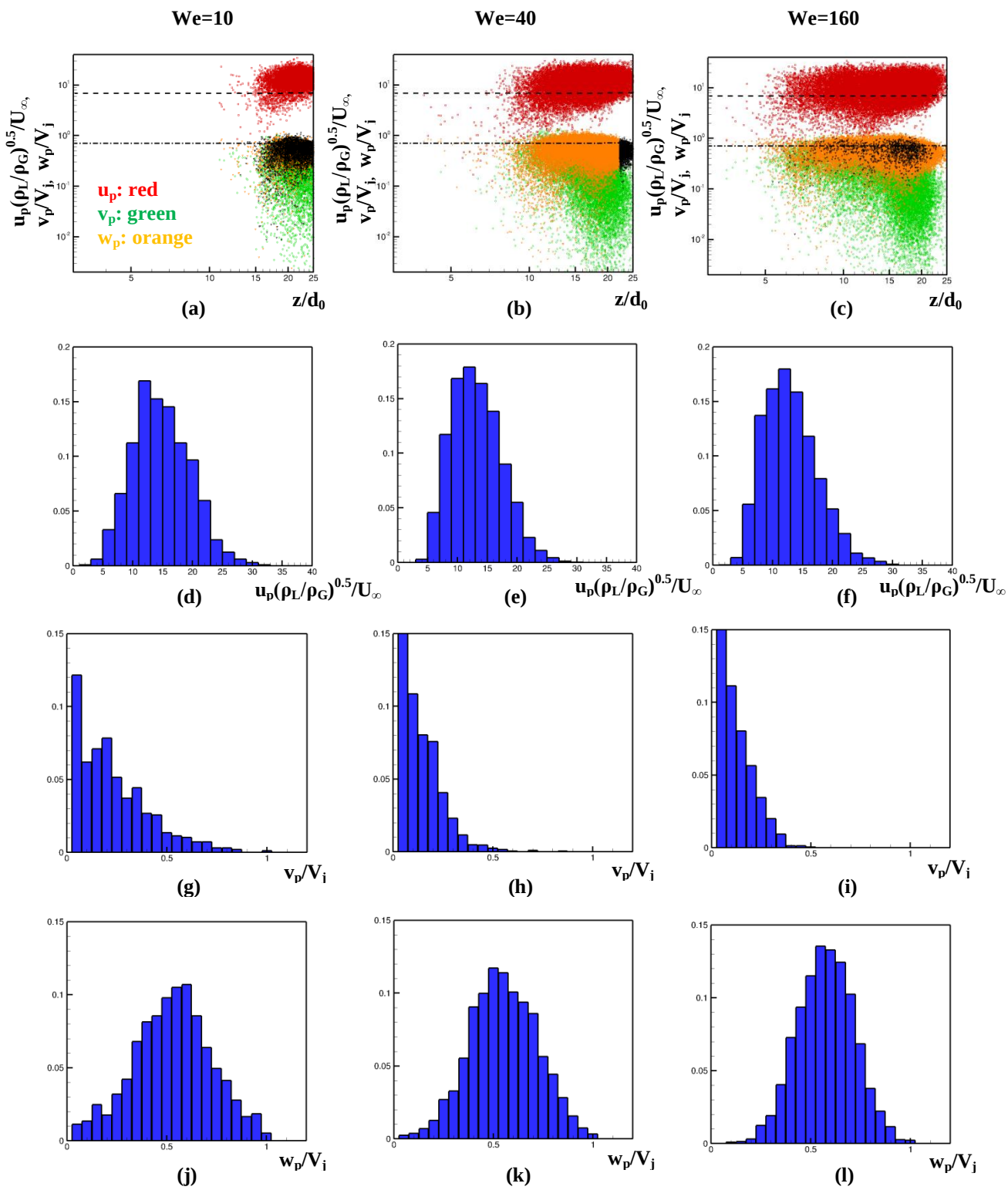

Figure 12. (a)-(c) shows droplet velocities along z coordinates at different We. Experimental correlation x (dashed line) and z (dash-dotted line) velocity components by Sallam et al. [1] is also shown. (d)-(l) shows corresponding droplet velocity probability distribution at z/d_0=20.

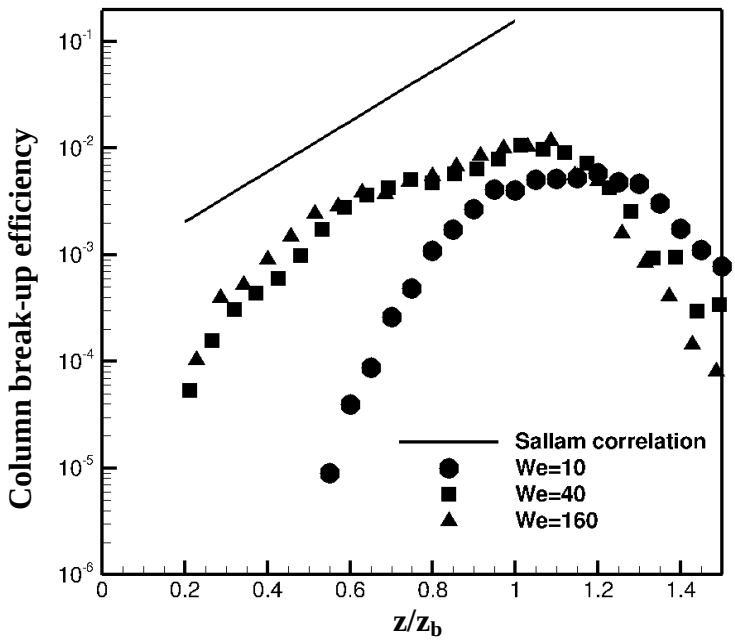

Figure 13. Efficiency of droplet generation along z direction.